Azimuthal magnetic field distribution in gas-puff Z-pinch implosions with and without external magnetic stabilization

N. Aybar [1], M. Dozieres [1], D. B. Reisman,[1] M. Cvejić,[2] D. Mikitchuk,[2] F. Conti,[1] E. Kroupp [2], R. Doron,[2] Y. Maron,[2] and F. N. Beg[1]

[1]*Center for Energy Research and Department of Mechanical and Aerospace Engineering, University of California San Diego, La Jolla, California 92093, USA*
[2]*Weizmann Institute of Science, Rehovot 7610001, Israel*

An experimental study of the magnetic field distribution in gas-puff Z pinches with and without a preembedded axial magnetic field (B_{z0}) is presented. Spatially resolved, time-gated spectroscopic measurements were made at the Weizmann Institute of Science on a 300 kA, 1.6 μs rise time pulsed-power driver. The radial distribution of the azimuthal magnetic field, B_θ, during the implosion, with and without a preembedded axial magnetic field of $B_{z0} = 0.26$ T, was measured using Zeeman polarization spectroscopy. The spectroscopic measurements of B_θ were consistent with the corresponding values of B_θ inferred from current measurements made with a B-dot probe. One-dimensional magnetohydrodynamic simulations, performed with the code TRAC-II, showed agreement with the experimentally measured implosion trajectory, and qualitatively reproduced the experimentally measured radial B_θ profiles during the implosion when $B_{z0} = 0.26$ T was applied. Simulation results of the radial profile of B_θ without a preembedded axial magnetic field did not qualitatively match experimental results due to magneto-Rayleigh-Taylor (MRT) instabilities. Our analysis emphasizes the importance of MRT instability mitigation when studying the magnetic field and current distributions in Z pinches. Discrepancies of the simulation results with experiment are discussed.

I. INTRODUCTION

Gas-puff Z pinches have been a long-utilized experimental platform for studying various aspects of plasma physics and radiation science including astrophysical plasmas, nuclear fusion, and basic plasma physics [1–3]. In a Z pinch, a cylindrical column of plasma is compressed on its central axis by the $\mathbf{J} \times \mathbf{B}$ force arising from the interaction of a current pulse with its self-generated magnetic field. The efficacy of Z pinches for nuclear fusion or high energy-density science applications depends on proper parametrization of the driving current and magnetic field, especially for nuclear fusion [1]. Knowledge of the evolution of the spatially varied magnetic field and current density is essential to achieve a comprehensive understanding of Z-pinch implosions [2–5].

Various techniques have been used in measuring magnetic fields in Z pinches, each with its respective strengths and weaknesses. Faraday rotation has produced spatially resolved magnetic field measurements in Z pinches but requires spatially resolved density measurements and is limited to electron densities less than $\sim 10^{19}$ cm^{-3} [6–8]. Proton deflectometry can provide two-dimensional (2D) maps of magnetic fields in Z pinches but relies on complex particle tracing simulations and requires a source of MeV protons to make such measurements [9,10]. Zeeman-based spectroscopic techniques are an attractive, noninvasive measurement of the magnetic fields in Z pinches, predominantly limited by spectral line broadening mechanisms, namely, Stark broadening, which render Zeeman

splitting unresolvable. To overcome this limitation, the polarization properties of Zeeman splitting have been exploited and advanced upon for the past few decades [11–13]. Such spectroscopic techniques in the visible spectrum have made recent advancements, yielding additional insight into Z-pinch dynamics regarding the current distribution in stagnating plasmas and the effect of an axial magnetic field on the current distribution during the implosion phase [13,14].

Z pinches have been known to develop instabilities known as "kink" and "sausage" modes as well as the magneto-Rayleigh-Taylor instability (MRTI) [1,2,15]. These instabilities can be significantly mitigated by applying an external axial magnetic field (B_{z0}) [1,2,16–19]. Measurements of the azimuthal magnetic field (B_θ) have also shown that an initial axial magnetic field may cause a redistribution of current to larger radii [14]. Spatially resolved measurements of B_θ during stagnation (the period during the experiment characterized by a peak in radiative emission) of gas-puff Z pinches have shown that only a fraction of the total current flows within the stagnating plasma and that the overall radial distribution of B_θ disagrees with magneto-hydrodynamic simulations [13]. The Z-pinch implosions presented here were specifically designed to suppress the peripheral low-density plasma (LDP) effect which can cause such current redistribution [14].

This paper will add to the body of information gathered in the aforementioned studies [11–14] to include spatially resolved measurements of B_θ in oxygen Z pinches with an

externally applied axial magnetic field. We examine the effect of the axial magnetic field on the azimuthal magnetic field distribution within the imploding plasma. The remainder of the paper is organized as follows: Section II discusses the experimental setup and briefly describes the magnetohydrodynamics (MHD) model. Section III compares experimental and simulation results. Section IV contains concluding remarks.

II. EXPERIMENTAL SETUP AND MODELING DETAILS

The experiment was carried out at the Weizmann Institute of Science in Rehovot, Israel. This section will first cover the driver and diagnostics used in the experiment, then briefly describe the methodology of spectroscopic determination of the azimuthal magnetic field, and, finally, detail the magneto-hydrodynamic (MHD) simulation setup.

A. Experimental setup

The pulsed-power driver consisted of a 16 μF capacitor bank charged to 23 kV and delivered a peak current of ~300 kA into a plasma load with a rise time of 1.6 μs. An annular gas-puff system was used to produce a hollow oxygen gas shell with a ~38 mm outer diameter and a ~14 mm inner diameter between an anode-cathode gap of 10 mm. The injector nozzle also featured a central gas nozzle that was not used during the experiment presented here. A pair of Helmholtz coils residing outside of the vacuum chamber were pulsed 95 ms prior to the start of the plasma current driver to impose an approximately uniform axial magnetic field of 0.26 T in the load region. An initial axial magnetic field of ~0.1 T is expected to significantly improve the pinch stability [20,21]. A long pulse was required to allow the axial magnetic field to penetrate the vacuum chamber and anode-cathode gap. Prior to data collection, several (about five) "cleaning" discharges of the Z-pinch pulsed-power driver were performed to remove adsorbates from the electrodes to minimize the current loss from the imploding plasma to a low-density plasma potentially generated by electrode contaminants.

The implosion timescale is around 700 ns after the onset of the current pulse which was determined using the ultraviolet-visible emission signal detected with a photodiode and fast oscilloscope. For each discharge, a B-dot probe located at a radius of 12 cm, and $z = 5$ mm, where $z = 0$ corresponds to the exit plane of the injector nozzle, was used to infer the circuital current. A sample current trace and photodiode signal are shown in Fig. 1.

The diagnostics used in this experiment are shown in Fig. 2. A visible-near-ultraviolet (UV) imaging spectrometer coupled to a time-gated intensified charge-coupled device (ICCD) camera was used to determine the azimuthal magnetic field using methods reported in the literature [22,23] and described in Sec. II B. This spectrometer featured a 2400 grooves/mm grating providing a spectral resolution of 0.4 Å and range from 3775 to 3820 Å. A system of relay optics and a bifurcated optical fiber array was used to couple the plasma emission to the spectrometer with a spatial resolution of ~0.7 mm in the radial direction. The detector was a time-gated ICCD using a 30 ns gate time. A separate time-gated ICCD provided images of visible light emitted by the plasma
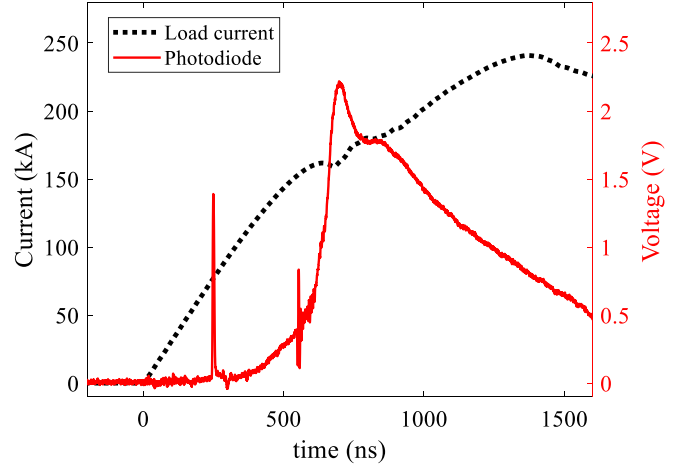

FIG. 1. Profile of load current and response of UV-visible photodiode. The inductive current notch and peak photodiode signal occur close to 700 ns. The photodiode peaks at 250 and 555 ns are signals from timing monitors for the laser and imaging ICCD, respectively.

[24]. This signal was integrated over 5 ns and allowed for determination of the plasma radius and stability of the plasma-vacuum boundary. Finally, a second visible-near-UV imaging spectrometer also coupled to a time-gated ICCD camera provided spectroscopic data used to determine the ionization state distribution and a measurement of electron temperature T_e.

B. Method of determining B_θ

To measure the magnetic field in Stark-dominated conditions, a Zeeman-based spectroscopic technique utilizing the polarization properties of line emission parallel to the magnetic field was used. In the presence of a magnetic field, atomic energy levels are split according to

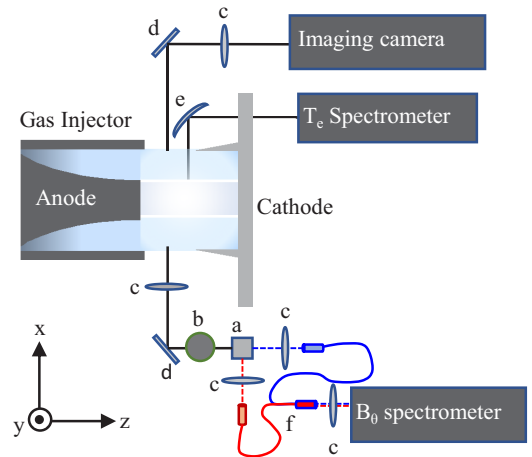$$\Delta E = M_i g_{Li} \mu_B B, \tag{1}$$

FIG. 2. Diagram of the experimental arrangement. The elements are as follows: (a) polarizing beam splitter cube, (b) $\lambda/4$ wave plate, (c) lenses, (d) flat mirrors, (e) spherical mirror, and (f) bifurcated fiber bundle.
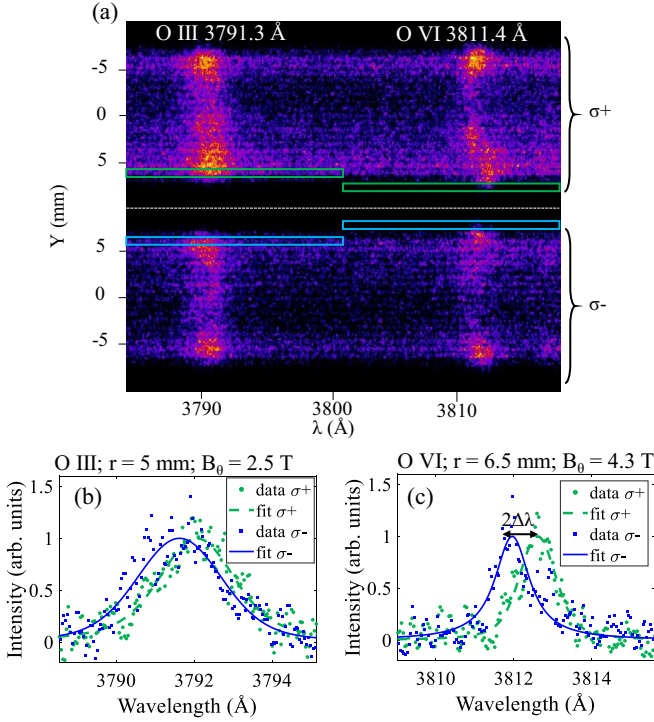
FIG. 3. Example of a spectral image for B_θ measurement (a). The rectangles correspond to the positions from which the spectral sample was taken and correspond to the edge of emission for that spectral line. Plots of the lineouts are shown for O III (b) and O VI (c).

where M_i is the magnetic quantum number of level i, g_{Li} is the Landé g factor of level i, μ_B is the Bohr magneton, and B is the magnetic field strength. In the simplest case of Zeeman splitting, a spectral line emitted in the presence of a magnetic field will be split into two lines separated from the unperturbed wavelength by

$$\Delta\lambda = 4.669 \times 10^{-9}[M_q g_{Lp} - M_p g_{Lp}]\lambda_0^2 B, \qquad (2)$$

with $\Delta\lambda$ measured in Å, where λ_0 is the unperturbed wavelength of the transition in Å, B is the magnetic field strength in teslas, and p and q are the upper and lower energy levels involved in the transition [25]. The $\sigma+$ and $\sigma-$ Zeeman components of the spectral line will each be circularly polarized with opposite handedness when viewed parallel to the magnetic field (at the edge of the plasma column). The optical system shown in Fig. 2 is designed to separate the $\sigma+$ and $\sigma-$ Zeeman components. A $\lambda/4$ wave plate converts the circularly polarized light into linearly polarized light, and then the orthogonal linear polarizations are separated with a polarizing beam splitter cube and subsequently sent to the high-resolution spectrometer via a bifurcated fiber array. Each array is comprised of 50 mapped fibers, with each fiber collecting light from a plasma volume 0.7 mm across. As shown in Fig. 3(a), the signals are symmetrically split on the ICCD. Figures 3(b) and 3(c) show pairs of spectral lineouts taken from the O III and O VI transitions, respectively. The signals shown in Figs. 3(a) and 3(c) are normalized to the maximum intensity values of the Voigt profile for each polarization.

From each image, a sample lineout is made near the edge of emission of the plasma where the line of sight is parallel to B_θ. The sample size in the radial direction for each lineout is ten pixels, corresponding to the view of one fiber, or ~0.7 mm in the plasma. Lineouts are taken from the center of the CCD image to avoid the effect of vignetting. All emission lines are then fitted to a Voigt profile, where the Lorentzian contribution accounts for the Stark broadening, and the Gaussian contribution represents the thermal Doppler and instrumental broadening. Note that each transition used for this experiment produces a Zeeman pattern, consisting of several $\sigma+$ and $\sigma-$ lines, each characterized by a pair of $M_i g_{Li}$ values. However, the Zeeman pattern is unresolved, and the spectrometer only detects two lines for a given ion (one for $\sigma+$, one for $\sigma-$), each comprised of all the unresolved lines. An average of the $\Delta M g_L$ values is used to consider the group of unresolved individual σ lines in Eq. (2). B is then calculated using this average and the difference in the central wavelength position of each fitted Voigt profile which corresponds to $2\Delta\lambda$. For the O III $\lambda = 3791.26$ Å transition, a $\Delta\lambda$ value of 0.090 Å corresponds to $B_\theta = 1$ T while for the O VI $\lambda = 3811.35$ Å transition, $B_\theta = 1$ T for $\Delta\lambda = 0.076$ Å. The uncertainty in the measurement is determined by the 95% confidence bounds of the central wavelength positions determined by using the Voigt fitting.

The spectral range of the diagnostic system is set to capture both O III $3s\,^3P_2 - 3p\,^3D_2$ at 3791.26 Å and O VI $3s\,^3S_{1/2} - 3p\,^2P_{3/2}$ at 3811.35 Å as shown in Fig. 3. It is important to note that not all the shots produced O VI lines as portrayed in Fig. 3. O VI only appeared after 60 ns prior to stagnation. When both transitions were detected, two lineouts (one per ionization state) were made for each polarization. This configuration allowed for a measurable radial distribution of B_θ. The use of multiple charge states in conjunction with polarization-based Zeeman splitting has been demonstrated previously [13,23].

Finally, each B_θ measurement presented in this paper has been made at one specific axial position in the plasma column. In lieu of axially resolved measurements, shots were repeated to collect spectral data from different axial positions ranging from $z = 1$ mm to $z = 7$ mm away from the nozzle, as illustrated in Fig. 2.

C. MHD simulations

Calculations were performed with TRAC-II, a 2D azimuthally symmetric radiation magnetohydrodynamic (MHD) code [26]. In Lagrangian codes such as TRAC-II, mesh tangling can become problematic if MRTI growth is significant. For this reason, the simulations were run in one-dimensional (1D) Lagrangian mode and were driven by the experimentally measured current waveform. TRAC-II uses the quotidian equation of state model (QEOS) [27]. The QEOS model reduces to the ideal gas law for high temperatures ($T \gg T_{\text{melt}}$) and low densities ($\rho \ll \rho_{\text{solid}}$). The Lee-More model [27] is used for electrical and thermal conductivities. The Lee-More model for a plasma approximates the Spitzer resistivity with corrections that depend on the magnetic field, the chemical potential, and ionization fraction. A single-group radiation model is used with tabular Rosseland and Planck opacities. The initial gas

density profiles used in the simulations were scaled from interferometric measurements of argon gas puffs, the process of which is described in Ref. [28]. Since mass density profiles were not characterized for O_2, MHD simulations were initialized assuming a similar profile structure. To estimate the appropriate initial density profile, the argon measured profile was scaled so that the simulated peak compression time approximately matched the stagnation time observed in experiment. This was achieved with an initial linear mass density of $\sim 1.2 \times 10^{-5}$ g/cm.

III. RESULTS AND DISCUSSION

This section will cover the results obtained from both the experimental data and MHD simulations. Section III A will contain results focusing on the implosion dynamics. Section III B will cover the evolution of B_θ at the outer plasma radius, and Section III C will present experimental and simulated results of the radial distribution of B_θ.

A. Implosion dynamics

The images obtained from the time-gated ICCD provided measurements of the outer plasma radius in the visible range and instability growth over the course of the implosion. An example of such images is presented in Fig. 4, where the top four images featured the applied axial magnetic field, and the bottom four did not. Qualitatively, the images for the case with initial axial magnetic field (B_{z0}) show no significant growth of current driven instabilities or the magneto-Rayleigh-Taylor instability and present a roughly uniform plasma column near stagnation. On the other hand, instability growth is clearly apparent in images where $B_{z0} = 0$. The absence of instability mitigation reduces the shot to shot reproducibility of the implosion.

Combining data from dozens of shots provides an evolution of the radius for all observed z positions with and without external applied B field, as shown in Fig. 5. Measurements of the outer plasma radius were made by axially integrating the intensity from $z = 3$ to 9 mm from the anode to avoid edge effects observed near the injector nozzle at $z < 3$ mm. The outer plasma radius is defined by the full width at half maximum intensity of the horizontal lineout of the image. These data are compared with the one-dimensional simulation results from TRAC-II. The simulation peak compression (the point in time during the simulation characterized by a minimum outer radius) occurred at 682 and 673 ns for cases with and without B_{z0}, respectively. The experimentally determined stagnation times agreed well with the simulations, occuring at 697 ± 15 ns in the cases with B_{z0}, and 660 ± 15 ns without. The times reported in Fig. 5 are referenced to the stagnation time for each respective shot. Note that the peak photodiode signal coincides with the minimum plasma radius to within 10 ns.

The simulations with $B_z = 0$ show a minimum radius of ~ 0.5 mm, a significantly lower value than measurements made near stagnation time. Measurements of the plasma radius taken from several shots within ± 25 ns of stagnation produced an average value of 2.9 ± 1.2 mm (1 σ) for $B_{z0} = 0$ and 3.2 ± 1.1 mm (1 σ) for $B_{z0} = 0.26$ T. Considering that the measurements of the outer plasma radius were made with
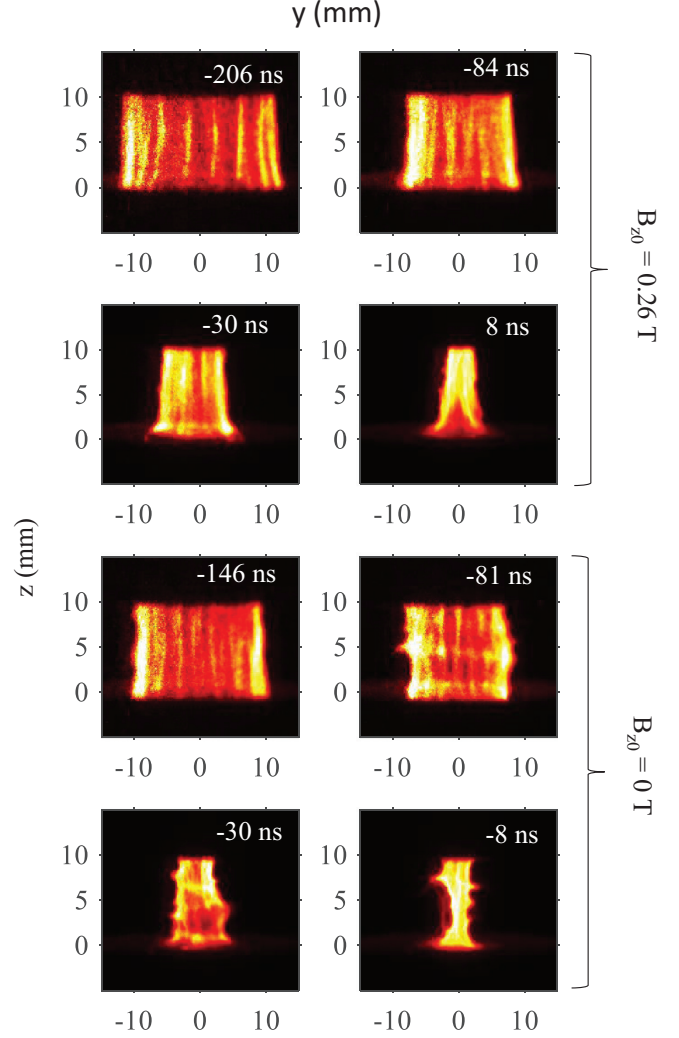

FIG. 4. Images obtained from the time-gated ICCD for eight shots, each taken at different times relative to the pinch. The top four images correspond with B_{z0} and the bottom four without B_{z0}. The $z = 0$ mm position corresponds to the edge of the nozzle injector (anode).

~ 6 mm axial integration, any present instability structures were averaged over when determining the outer plasma radius from the images. Since the 1D simulations cannot incorporate instabilities present in the experiment, the compression is overestimated, resulting in the smaller minimum radius. Overall, the implosion dynamics is well captured by the 1D simulations considering the overall implosion trajectory. However, the measured outer radius is consistently larger than simulation predictions by 1.25 mm on average between -60 and 0 ns. While the evolution of the plasma dynamics is overall well reproduced by the TRAC-II simulations, it is important to keep this discrepancy in mind when comparing B_θ measurements to simulations in Sec. III C. Comparison between experimental data and simulation results suggests that some additional effects, besides counterpressure of B_z, are slowing down the plasma implosion. Additionally, the uncertainty in the estimated initial mass density profile used to initialize the simulations may be partly responsible for the
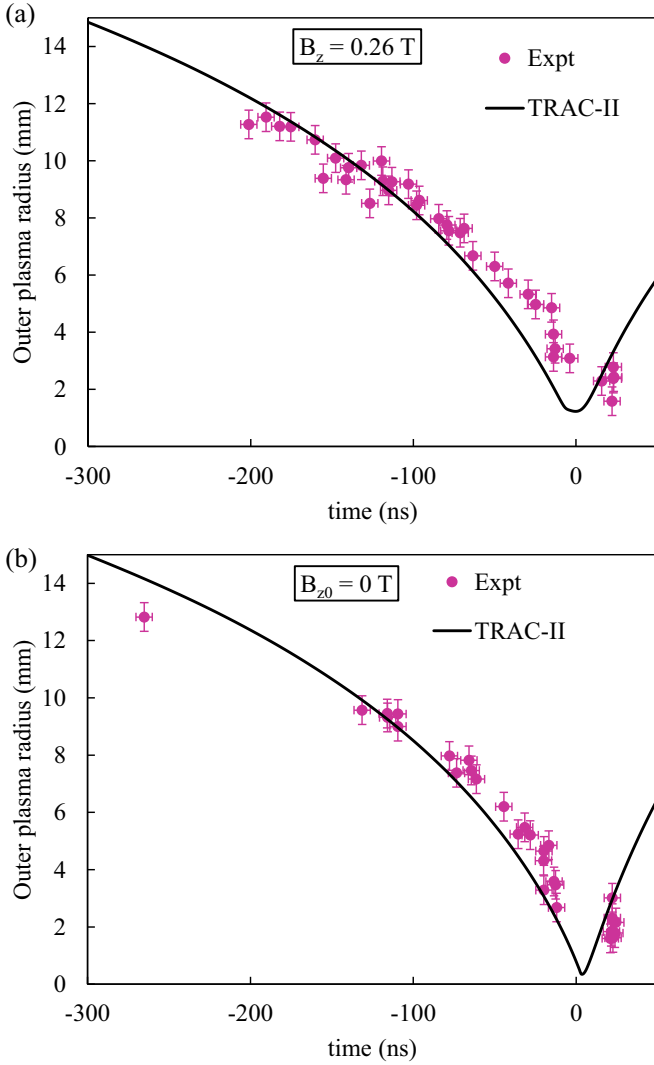
FIG. 5. Implosion trajectories for cases with and without initial axial magnetic field. Each data point is taken from a separate shot and axially integrated between 3 and 9 mm from the anode. The horizontal error bars correspond to the 5 ns integration time of the detector while the vertical error bars account for the resolution limitation of the imaging camera. The solid curves represent the motion of the outer plasma radius from the TRAC-II simulation results.

discrepancy between experimental and simulated implosion trajectories.

B. Evolution of azimuthal magnetic field

This section discusses the evolution of the azimuthal magnetic field at the outer edge of the plasma, corresponding with the radii discussed in Sec. III A and shown in Fig. 5. The evolution of the measured azimuthal magnetic field (B_θ) is shown in Fig. 6 for the cases with and without B_{z0} and compared to the values of B_θ calculated using Ampere's law: $B_\theta = \mu_0 I / 2\pi r_o$ where I is the circuital current measured with the B-dot probe and r_o is the measured outer plasma radius as defined by the outermost radial position at which the spectroscopic measurement could be made. The horizontal position of the measured values of B_θ corresponds to the time relative
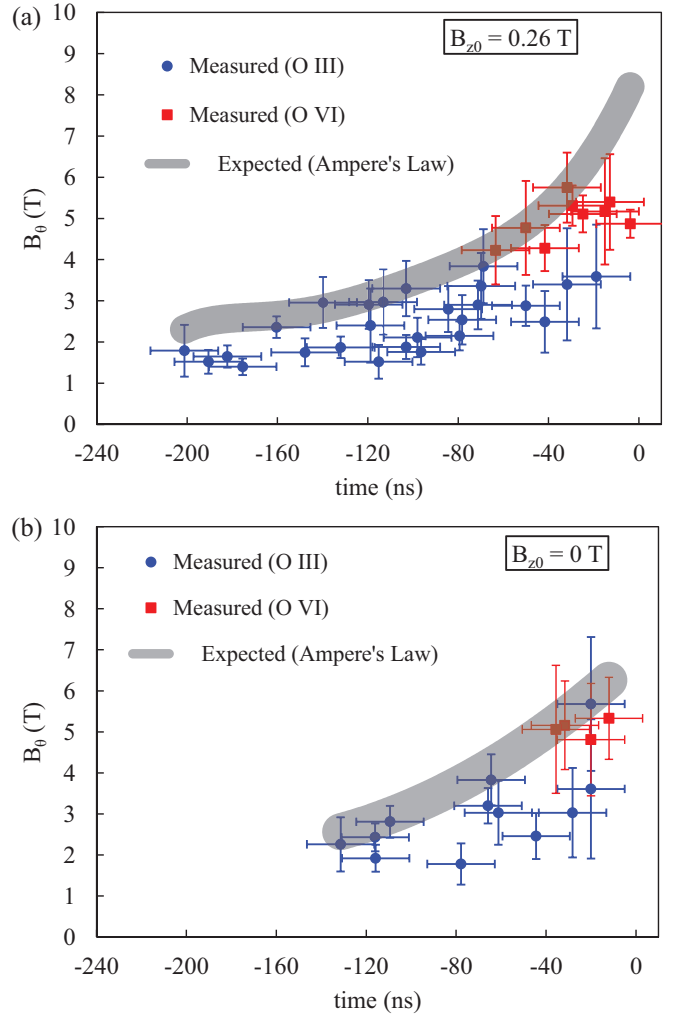

FIG. 6. Evolution of B_θ at the outer plasma radius for the cases (a) with a preembedded axial magnetic field and (b) without a preembedded axial magnetic field. The expected (Ampere's law) curve represents the range of calculated values of B_θ based on the B-dot measured current and outer plasma radius at the time of the B_θ measurement. The horizontal error bars correspond to 30 ns integration time of the detector.

to stagnation at which the spectral measurement was taken. For ease of viewing, the range of calculated B_θ values are presented as wide gray curves shown in Fig. 6. All data points presented in Fig. 6 were calculated using a spectral outline taken within 0.5 mm of the measured outer plasma radius.

While we can see in Fig. 6 that many points agree with the expected results, indicating that all of the current is flowing within those radial positions, several experimental values of B_θ remain lower than calculated. It is possible that a fraction of the current is carried by peripheral plasma at radii greater than the apparent plasma-vacuum boundary at which the spectroscopic measurement was made. It has been seen in Refs. [11,13,23] that there exists a radial ionization state distribution. The charge-state distribution observed in our plasmas shows that higher ionization states reside at larger radii. As the implosion progresses, the ionization state distribution evolves, and emission from O VI is observed in

B_θ measurements past 60 ns prior to the stagnation time with or without initial B_{z0}, as seen in Fig. 6 (red square data points). The O VI emission also provided B_θ values similar to the ones expected according to Ampere's law, while O III emission mainly shows points below the expected B_θ values. However, when only O III was observed on the B_θ spectrometer, the spectrometer dedicated to T_e measurement detected O IV and O V lines at radii beyond the apparent outer edge of the plasma. This observation indicates that a plasma composed of higher ionization states at larger radii is carrying part of the current, which explains the lower than expected B_θ values found for O III in Fig. 6. Note that the highest "expected" values shown in Fig. 6(b) are less than the highest expected values in Fig. 6(a), even though a smaller minimum radius is expected where $B_{z0} = 0$. This is due to the fact that the data collected for cases where $B_{z0} = 0$ were not taken as close to stagnation as some of the $B_{z0} = 0.26$ T data.

In cases where O VI is apparent on the B_θ measurement, the measured values of B_θ inferred from the O VI emission line are in good agreement with the calculated values until within ∼20 ns of the pinch, indicating that the current is, in those cases, fully flowing within the outer edge defined by the imaging camera until times near stagnation where potential higher ionization states might exist.

Finally, it is important to note that during this experiment we did not observe significant differences between expected and measured B_θ for the case with initial $B_{z0} = 0.26$ T and for the case without B_{z0}, as can be seen in Fig. 6. However, in Ref. [14] the effect of the axial magnetic field on a similar experiment has shown a stark contrast between discharges with and without B_{z0}. The results shown in Ref. [14] indicate that a low-density peripheral plasma was responsible for current loss in the imploding plasma. According to Ref. [14], the low-density peripheral plasma may have been the result of discharged material introduced from the pulsed Helmholtz coils within the vacuum chamber. It was noted that placing the Helmholtz coils outside of the vacuum chamber helped to mitigate the development of low-density peripheral plasma and the subsequent current losses. To minimize such losses, the data gathered for the present paper were collected using outwardly located Helmholtz coils. As a result, we observed no significant difference between the measured and expected values of B_θ both with and without $B_{z0} = 0.26$ T. In addition to the location of the Helmholtz coils, performing several "cleaning" discharges of the Z-pinch current driver both with and without B_{z0} can help to liberate and remove contaminants present on the surfaces of the current driver electrodes which is also important in mitigating current losses.

C. Radial distribution of azimuthal magnetic field

To further understand the current distribution in imploding gas-puff Z pinches, we utilize the ionization state distribution to construct a radial profile of the azimuthal magnetic field. Between ∼80 and ∼20 ns prior to stagnation, we have simultaneously observed emission from O III $3s\,^3P_2$–$3p\,^3D_2$ and O VI $3s\,^3S_{1/2}$–$3p\,^2P_{3/2}$ whose edge of emission appeared at different radii. Figure 7 shows the experimental B_θ values for a given shot at different radial positions compared with simulated B_θ radial distributions. Each color corresponds to
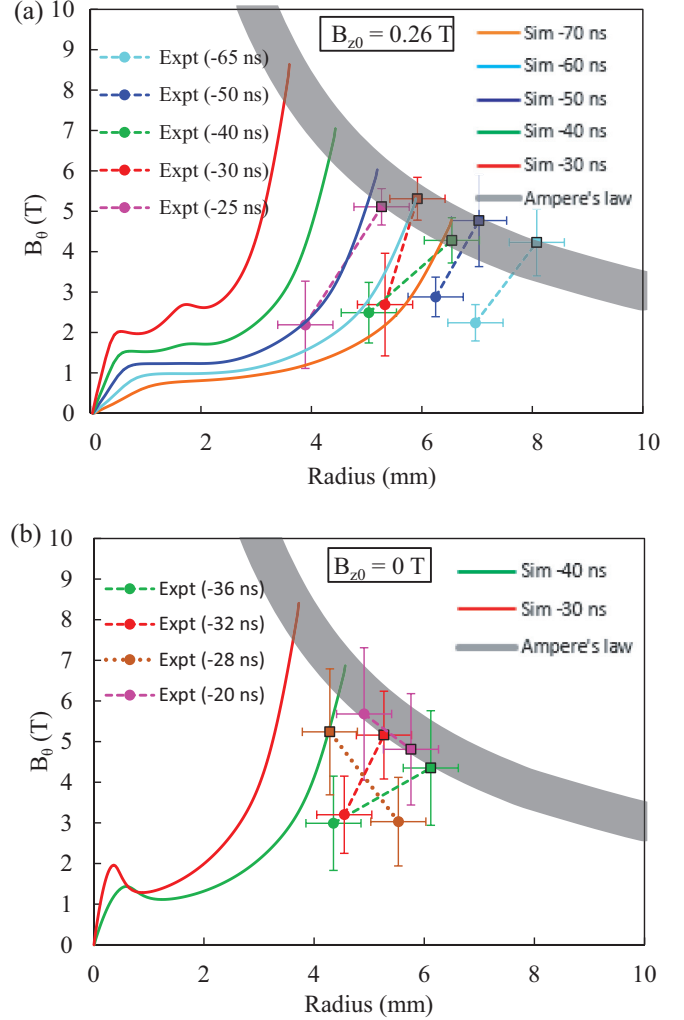

FIG. 7. Measured (dashed lines with points) and simulated (solid lines) radial profiles of the azimuthal magnetic field for various points in time for experiment and simulation with (a) axial magnetic field and without (b). The wide band of the gray curve denoted as "Ampere's law" is such to account for the range of current values measured for all discharges. Circular points were measured from O III, while square points were measured from O VI.

a point in time relative to pinch, both for experiment and simulations. The wide gray curve represents the expected B_θ according to Ampere's law for the range of current values associated with each data point and values of the outer plasma radius. The dashed lines in Fig. 7 connect two measured values obtained from the same shot.

In all presented cases, the outer plasma radius as measured by the imaging camera typically lies between the emission edges of O III and O VI, with the latter almost always located further out. Note that for each of the cases shown, the outermost measurement taken at the edge of the O VI emission corresponds to the value expected at that radius given the B-dot current measurement using Ampere's law.

In the case with an externally applied axial magnetic field [Fig. 7(a)], the measured B_θ profiles are lower than the simulated values for each given time and systematically appear at greater radii, resulting in an apparent time shift

between measured and simulated profiles in Fig. 7(a). For example, the measured profile at −30 ns (red data points) matches the simulation profile around −60 ns. The simulations have been shown in Sec. III A to overpredict axially averaged plasma compression at times between −70 and 0 ns. Because of this overestimation, the simulated plasma radius is smaller than the measured values, and the corresponding values for B_θ are necessarily overpredicted. Since all of the measured radial profiles of B_θ were taken later than −70 ns, this discrepancy between simulation and experiment is apparent for all profiles shown in Fig. 7(a). Looking past this discrepancy, the measured B_θ data accurately follow the same profiles as the simulation results. Overall, this means that the physics of these pinches with B_{z0} are well captured by 1D MHD calculations. Implosions with $B_{z0} = 0.26$ T also indicate a high degree of azimuthal symmetry and an accurate model of magnetic diffusion.

Experimental data confirm a high degree of azimuthal symmetry where $B_{z0} = 0.26$ T. Values of B_θ measured at the opposite azimuth differed on average by only 18% for discharges where $B_{z0} = 0.26$ T and differed on average by 32% with no axial magnetic field. It should be noted that the emission intensity is highly asymmetric when $B_{z0} = 0$, often resulting in a higher uncertainty of B_θ measured from the opposite azimuth. In addition, the model of magnetic diffusion is further verified by agreement between experimental and simulated resistivity values. Mass averaged resistivity values obtained from 1D simulations were of the order 1×10^{-5} Ω m, while the Spitzer resistivity value for the estimated plasma temperature of 10 eV during the implosion phase of the experiment was 1.8×10^{-5} Ω m. Line intensity ratios of O III to O V transitions provide an estimate of T_e between 8 and 12 eV during the implosion phase based on Saha equilibrium. The skin depth associated with this resistivity value and the current driver frequency is ∼5.2 mm, in good agreement with the apparent current sheath thickness presented by the measured B_θ profiles.

In the case with no axial magnetic field, the measurements and simulations do not, in general, agree. The radial distribution inside the plasma does not follow the same shape as the case with the preembedded axial magnetic field and is not consistent between discharges. Nonmonotonic distributions of B_θ have previously been observed in implosions without axial magnetic field stabilization in Ref. [13] where it has been proposed that this observation may be due to flaring of the plasma caused by instability structures. While this may be the case in the experiment presented here, such large flaring seen in Ref. [13] was not observed for the discharges presented in Fig 7(b). In our experiment, it is not certain that the diagnostic method is entirely valid where MRTI is present.

This diagnostic technique assumes that the magnetic field is parallel to the line of sight. The validity of this assumption requires that the data are taken at the edge of the emission of a particular line. It is important to remember that all measurements presented here are integrated along the line of sight. In cases where hydrodynamic instabilities are present, it is conceivable that the complex three-dimensional structure of such instabilities may lead to collection of emission from plasma protruding at adjacent azimuthal positions, partially invalidating this important assumption.

In addition, spatial gradients may induce a nonhomogeneous charge-state distribution affecting the current path. In fact, in one case shown in Fig. 7(b), at −28 ns, the charge-state distribution is reversed, with O III appearing at a larger radii than O VI. In this case, the peak magnetic field strength appears at a smaller radius than the measured outer radius. A possible explanation for this phenomenon, assuming that the measurement is valid, is that hydrodynamic instabilities cause regions of plasma to displace one another, not only reversing the charge-state distribution locally, but transporting magnetic flux inward, creating an inverted magnetic field distribution on the spatial scale of the measurements (∼3 mm). Furthermore, the MRT instability structure will likely result in an axially dependent radial distribution of the current, and thus of B_θ, where MRT structures are pronounced. More experimental data would be required to investigate this interesting phenomenon further. For example, duplicating diagnostic systems to simultaneously measure B_θ from multiple azimuthal positions would provide more clear information on the azimuthal asymmetry.

IV. CONCLUSION

Gas-puff Z-pinch experiments with and without an initial axial magnetic field were performed at the Weizmann Institute of Science where the evolution of the azimuthal magnetic field distribution was measured using a polarization-based spectroscopic technique. All measurements were spatially resolved along the radius, integrated along the line of sight and time gated.

The measured evolution of B_θ at the outer plasma radius gave valuable insight about the current distribution, confirming work from previous studies that nearly all the current flows within the plasma radius defined by the higher ionization state emission which is not always visible with diagnostics such as a simple imaging camera. Our results show the importance of defining the ionization distribution over time in Z-pinch plasma experiments in order to determine the current distribution more accurately.

We compared the measured B_θ radial distribution with and without initial magnetic field and showed that better qualitative agreement between the MHD simulations and experimental results is found in the implosions where $B_{z0} = 0.26$ T than where $B_{z0} = 0$ T. Still, we observed an apparent discrepancy between the experimental data and the simulations due to the overestimation, by the latter, of the plasma compression in the final ∼70 ns of the implosion. However, the measured B_θ profiles without B_{z0} were not well reproduced by the simulations since the inhomogeneity of the plasma caused by instabilities is not produced in 1D simulations. In such cases, the analysis of B_θ measurements becomes increasingly complex and may require more data to accurately capture the plasma dynamics. While the implosion trajectories exhibit good reproducibility both with and without B_{z0}, the contrast between the clear behavior of the B_θ radial distribution when B_{z0} is applied and its low reproducibility without B_{z0} emphasizes the importance of stabilization in Z-pinch implosions for such measurements. Further investigation will require 2D simulations to address the development of MRTI and its effect on the magnetic field distribution in the plasma.

[1] D. D. Ryutov, M. S. Derzon, and M. K. Matzen, Rev. Mod. Phys. **72**, 167 (2000).

[2] M. G. Haines, Plasma Phys. Control. Fusion **53**, 093001 (2011).

[3] J. L. Giuliani and R. J. Commisso, IEEE Trans. Plasma Sci. **43**, 2385 (2015).

[4] F. S. Felber, F. J. Wessel, N. C. Wild, H. U. Rahman, A. Fisher, C. M. Fowler, M. A. Liberman, and A. L. Velikovich, J. Appl. Phys. **64**, 3831 (1988).

[5] M. R. Gomez, S. B. Hansen, K. J. Peterson, D. E. Bliss, A. L. Carlson, D. C. Lamppa, D. G. Schroen, and G. A. Rochau, Rev. Sci. Instrum. **85**, 11E609 (2014).

[6] A. V. Branitskii, V. D. Vikharev, A. G. Kasimov, S. L. Nedoseev, A. A. Rupasov, G. S. Sarkisov, V. P. Smirnov, V. Ya. Tsarfin, and A. A. Shikanov, Sov. J. Plasma Phys. **18**, 588 (1992).

[7] S. N. Bland, D. J. Ampleford, S. C. Bott, A. Guite, G. N. Hall, S. M. Hardy, S. V. Lebedev, P. Shardlow, A. Harvey-Thompson, and F. Suzuki, Rev. Sci. Instrum. **77**, 10E315 (2006).

[8] V. V. Ivanov, A. A. Anerson, D. Papp, A. L. Astanovitsky, V. Nalajala, and O. Dmitriev, Phys. Plasmas **22**, 092710 (2015).

[9] V. Munzar, D. Klir, J. Cikhardt, B. Cikhardtova, J. Kravarik, P. Kubes, and K. Rezac, IEEE Trans. Plasma Sci. **46**, 3891 (2018).

[10] D. Mariscal, C. McGuffey, J. Valenzuela, M. S. Wei, J. P. Chittenden, N. Niasse, R. Presura, S. Haque, M. Wallace, A. Arias, A. Covington, H. Sawada, P. Wiewior, and F. N. Beg, Appl. Phys. Lett. **105**, 224103 (2014).

[11] G. Davara, L. Gregorian, E. Kroupp, and Y. Maron, Phys. Plasmas **5**, 1068 (1998).

[12] R. Doron, D. Mikitchuk, C. Stollberg, G. Rosenzweig, E. Stambulchik, E. Kroupp, Y. Maron, and D. A. Hammer, High Energy Density Phys. **10**, 56 (2014).

[13] G. Rosenzweig, E. Kroupp, T. Queller, A. Starobinets, Y. Maron, V. Tangri, J. L. Giuliani, and A. Fruchtman, Phys. Plasmas **27**, 022705 (2020).

[14] D. Mikitchuk, M. Cvejić, R. Doron, E. Kroupp, C. Stollberg, Y. Maron, A. L. Velikovich, N. D. Ouart, J. L. Giuliani, T. A. Mehlhorn, E. P. Yu, and A. Fruchtman, Phys. Rev. Lett. **122**, 045001 (2019).

[15] E. G. Harris, Phys. Fluids **5**, 1057 (1962).

[16] F. Conti, N. Aybar, J. Narkis, J. C. Valenzuela, H. U. Rahman, E. Ruskov, E. Dutra, S. Haque, A. Convington, and F. N. Beg, Phys. Plasmas **27**, 012702 (2020).

[17] D. Mikitchuk, C. Stollberg, R. Doron, E. Kroupp, Y. Maron, H. R. Strauss, A. L. Velikovich, and J. L. Giuliani, IEEE Trans. Plasma Sci. **42**, 2524 (2014).

[18] F. S. Felber, F. J. Wessel, N. C. Wild, H. U. Rahman, A. Fisher, C. M. Fowler, M. A. Liberman, and A. L. Velikovich, Laser Part. Beams **5**, 699 (1987).

[19] F. S. Felber, M. M. Malley, F. J. Wessel, M. K. Matzen, M. A. Palmer, R. B. Spielman, M. A. Liberman, and A. L. Velikovich, Phys. Fluids **31**, 2053 (1988).

[20] A. B. Bud'ko, F. S. Felber, A. I. Kleev, M. A. Liberman, and A. L. Velikovich, Phys. Fluids **1**, 598 (1989).

[21] G. Peterson, Ph.D. thesis, University of California Irvine, 1994.

[22] R. P. Golingo, U. Shumlak, and J. Den Hartog, Rev. Sci. Instrum. **81**, 126104 (2010).

[23] G. Rosenzweig, E. Kroupp, A. Fisher, and Y. Maron, J. Instrum. **12**, P09004 (2017).

[24] D. Alumot, E. Kroupp, and A. Fisher, J. Instrum. **9**, P05004 (2014).

[25] H. J. Kunze, Line broadening, in *Introduction to Plasma Spectroscopy*, Springer Series on Atomic, Optical and Plasma Physics Vol. 54 (Springer-Verlag, Berlin, 2009), Ch. 9, p. 153.

[26] D. B. Reisman, A. Toor, R. C. Cauble, C. A. Hall, J. R. Asay, M. D. Knudson, and M. D. Furnish, J. Appl. Phys. **89**, 1625 (2001).

[27] R. M. More, K. H. Warren, D. A. Young, and G. B. Zimmerman, Phys. Fluids **31**, 3059 (1988).

[28] D. Mikitchuk, Ph.D. thesis, Weizmann Institute of Science, 2016.